

Intensity mapping without cosmic variance

Trevor M. Oxholm^{1,2,*} and Eric R. Switzer²

¹*Department of Physics, University of Wisconsin-Madison, Madison, WI, USA*

²*NASA Goddard Space Flight Center, Greenbelt, MD, USA*

Current and future generations of intensity mapping surveys promise dramatic improvements in our understanding of galaxy evolution and large-scale structure. An intensity map provides a census of the cumulative emission from all galaxies in a given region and redshift, including faint objects that are undetectable individually. Furthermore, cross-correlations between line intensity maps and galaxy redshift surveys are sensitive to the line intensity and clustering bias without the limitation of cosmic variance. Using the Fisher information matrix, we derive simple expressions describing sensitivities to the intensity and bias obtainable for cross-correlation surveys, focusing on cosmic variance evasion. Based on these expressions, we conclude that the optimal sensitivity is obtained by matching the survey depth, defined by the ratio of the clustering power spectrum to noise in a given mode, between the two surveys. We find that mid- to far-infrared space telescopes could benefit from this technique by cross-correlating with coming galaxy redshift surveys such as those planned for the Nancy Grace Roman Space Telescope, allowing for sensitivities beyond the cosmic variance limit. Our techniques can therefore be applied to survey design and requirements development to maximize the sensitivities of future intensity mapping experiments to tracers of galaxy evolution and large-scale structure cosmology.

I. INTRODUCTION

Intensity mapping is an emerging approach to studying galaxy evolution and large-scale structure cosmology. Intensity maps trace the cumulative emission of a given line from all galaxies within a region, making them sensitive to the line luminosity function without the selection effects present in direct-detection surveys. Due to modest aperture requirements and advancements in detector and spectrometer technologies, intensity mapping surveys can be used to economically map extremely large volumes of the Universe.

While the present generation of intensity mapping surveys are limited by instrument noise, coming generations will be limited by cosmic variance [1–3]. Cosmic variance is intrinsic to measurements of the power spectrum of a fluctuating field, and can only be improved by measuring a larger number of Fourier modes. Furthermore, variance in the matter density field leads to cosmic variance in the inference of the line intensity and clustering bias, owing to a degeneracy between the three parameters.

Cosmic variance can be avoided by cross-correlating the intensity map with another large-scale structure survey tracing the same matter density field [4–7]. Information from the cross-correlating survey can be used to break the degeneracy between the intensity and the matter overdensity. Furthermore, cross-correlation with a galaxy redshift survey is established as an approach to reject contamination in intensity maps from foregrounds and interloping lines, which do not correlate with emission from galaxy redshift survey population [8–10]. These sources of uncorrelated variance contribute to error bars in the cross-correlation but do not additively bias the result, as they would for intensity auto-correlations.

The formalism for cosmic variance evasion through cross-correlations has been well-developed in the context of weak lensing surveys [11]. Previous studies describe cosmic variance-free measurements of structure growth through redshift-space distortions [12] and primordial non-Gaussianity through scale-dependent biases [13]. While these studies provide a useful guide for intensity mapping cross-correlations, intensity maps are unique in their dependence on the line mass-luminosity function, as well as correlated shot noise between the two surveys. These unique features can be exploited to extend the cosmic variance evasion technique to measurements of galaxy evolution. Furthermore, the biased intensity can be extended to include scale-dependent bias and redshift-space distortions, thereby providing cosmic variance-free measurements of f_{NL} and the growth factor, respectively, as studied in Bernstein and Cai [12], Seljak [13].

Analysis of cross-correlation sensitivities may also be used to devise optimal survey strategies, in terms of survey depth or integration time per pixel. Cosmic microwave background (CMB) maps are analogous to intensity maps at discrete redshifts without the inclusion of a cross-correlating survey. Here, the error per mode is proportional to a cosmic variance term plus an instrument noise term, which decreases with increased survey depth. It is therefore optimal to increase the survey depth until cosmic variance provides the dominant source of variance, before focusing on increasing survey area to detect more modes; this conclusion matches that of Knox [14] regarding CMB sensitivities. For intensity mapping cross-correlations, on the other hand, variance per mode is optimized when the depths are matched between the intensity map and the cross-correlating map. Further details on the formalism are described in Section III.

We focus on intensity maps of singly-ionized carbon ([CII]). [CII] is of particular interest to studies galaxy

* oxholm@wisc.edu

evolution, owing to its reliable tracing of the star formation rate density and high brightness among cooling lines [15]. Furthermore, [CII] intensity maps may also provide powerful measurements of f_{NL} [16]. Pullen *et al.* [17] and Yang *et al.* [10] obtain preliminary detections of the [CII] mean intensity at $z = 2.6$. Dedicated experiments aim to follow up these measurements over a broad redshift range, including CCAT-prime [18], Concerto [19], EXCLAIM [20], TIM [21], and TIME [22]. Proposed next-generation space telescopes such as PIXIE [1, 23], GEP [24], and the Origins Space Telescope [25] may dramatically improve intensity mapping through far- to mid-IR lines, owing to the background-limited sensitivity of space platforms. We will focus on a realistic but generic space background-limited telescope for our forecasts.

While we study cross-correlations between [CII] intensity maps and galaxy redshift surveys, our techniques can be applied to any other intensity mapping cross-correlations, including those between two intensity maps. Particularly, this formalism can be applied to survey design and requirements development for future surveys limited by cosmic variance, analogous to the Knox Formula [14] describing CMB fluctuations. Furthermore, we show that these calculations are robust to additive biases in the intensity mapping power spectrum, which may be attributed to foregrounds or interloping lines.

We build on existing formalism from Switzer *et al.* [6] and Bernstein and Cai [12] for intensity mapping cross-correlations featuring correlated shot noise. We derive a simple expression for the cross-correlation sensitivity, and generalize the results to a variety of scenarios. We focus on cross-correlation between [CII] and a galaxy redshift survey. Finally, we describe optimal survey strategies based on our results.

II. INTENSITY MAPPING CROSS-CORRELATIONS

A. Tracing the matter density

The primary observable in an intensity map is the intensity field δ_I , which traces large-scale matter fluctuations δ_m as

$$\delta_I(\mathbf{r}, z) = I(z)b(z)\delta_m(\mathbf{r}, z), \quad (1)$$

where \mathbf{r} represents spatial location and b is the linear clustering bias of the observed galaxies relative to the underlying matter overdensity δ_m . $I(z)$ is the intensity at mean density, representing the cumulative emission from all galaxies in the survey region.

The intensity I is related to the first moment of the galaxy luminosity function, and its dependence on z probes galaxy evolution. Using the halo model approach [26], we calculate

$$I(z) = \alpha(z) \int_{M_{\text{min}}}^{\infty} L(M, z)n(M, z)dM \quad (2)$$

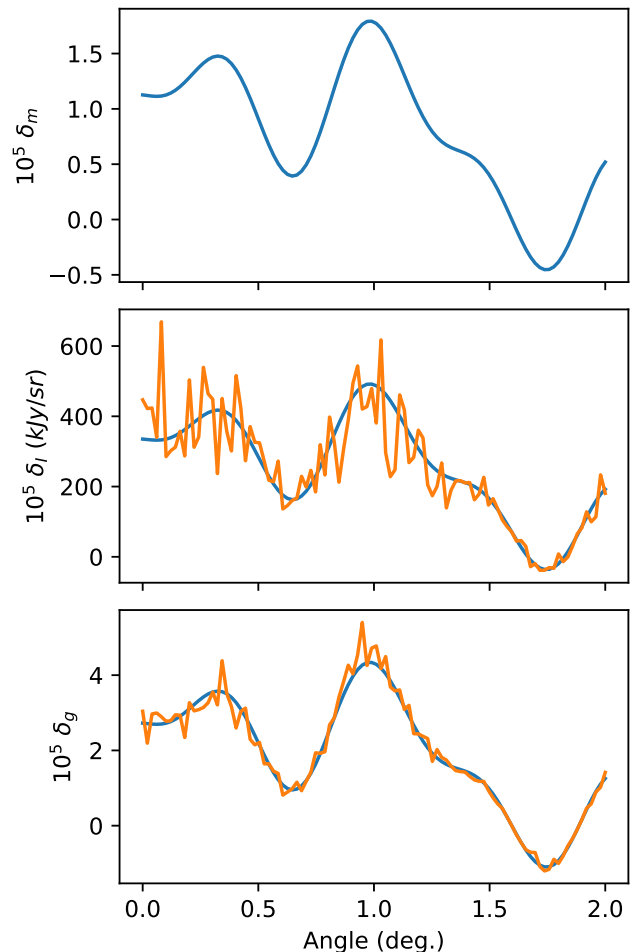


FIG. 1. Illustration of fluctuations in the overdensity of the matter (δ_m), intensity (δ_I), and galaxy (δ_g) fields. δ_I and δ_g trace the same matter overdensity δ_m according to Equations 1 and 5. The fields in the lower two panels are shown without noise (blue), and with fractional noise of 30% and 10% in δ_I and δ_g , respectively. Note that δ_m was constructed by superimposing 10 randomly-selected k modes of random phase, with amplitudes corresponding to amplitudes in the matter power spectrum.

where M is the halo mass and $n(M, z)$ is the halo mass function. $L(M, z)$ is the mass-luminosity relation for the given line, and is the primary observable that constrains galaxy evolution physics. M_{min} the minimum mass of a halo hosting a galaxy with the target line. Lower-mass halos tend to feature suppressed star formation activity, resulting in a negligible contribution to the mean line intensity [27]. We impose a strict halo mass cutoff of $M_{\text{min}} = 10^{10}M_{\odot}$ matching CIB models [28], though Equation 2 is not sensitive to order-of-magnitude changes in the halo mass cutoff, consistent with conclusions within Shang *et al.* [29]. Because we focus on large-scale clustering, our conclusions are not sensitive to changes in the halo mass profile that may be present on

smaller scales, which may be sensitive to M_{\min} through the halo occupation distribution.

The fractional prefactor $\alpha(z)$ is given by

$$\alpha(z) = \frac{1}{4\pi\nu_{\text{rest}}H(z)}, \quad (3)$$

accounting for the conversion from integrated luminosity to intensity (i.e. units of L_{\odot} to $\text{Jy sr}^{-1}\text{h}^{-3}\text{Mpc}^3$), and also accounts for luminosity distance and angular diameter distance effects. Here, ν_{rest} is the rest frame frequency of the target emission, and $H(z)$ is the Hubble parameter at redshift z .

The bias b between the intensity field and the underlying matter density field provides another observable that may be used to infer the mass-luminosity function. We calculate b as

$$b(z) = \frac{\int_{M_{\min}} dM b_h(M, z) L(M, z) n(M, z)}{\int_{M_{\min}} dM L(M, z) n(M, z)} \quad (4)$$

where $b_h(M, z)$ is the bias of a given halo against the underlying matter power spectrum [30, 31].

The intensity and bias are completely degenerate, so we group the terms together as the *biased intensity* $[Ib]$. In the calculations that follow, we define the biased intensity simply as the multiplication between the intensity I and a constant bias b , specified by Equations 2 and 4, without the inclusion of redshift-space distortions (RSD) or scale-dependent bias. $[Ib]$ therefore contains information about the integral of the line mass-luminosity function $L(M, z)$ and the halo mass cutoff M_{\min} . However, our formalism can be generalized to include RSD and scale-dependent biases in $[Ib]$ without significantly changing our conclusions. This generalization would provide information on structure growth, primordial non-Gaussianity, and nonlinear effects leading to scale-dependent biases on small scales. The mass of halos hosting star formation could also be measured through M_{\min} , benefiting from the use of RSD to separate I from b .

Using only information from the intensity map, $[Ib]$ is also degenerate with δ_m . The latter is subject to cosmic variance because it depends on the measurement of waves in the matter density field, with a variance limited by the number of observable modes. Because $[Ib]$ and δ_m are degenerate, cosmic variance in δ_m is coupled to variance in $[Ib]$.

The degeneracy may be broken through the inclusion of a second map tracing the matter overdensity, e.g. a galaxy redshift survey. In this case, the galaxy field δ_g is given by

$$\delta_g(\mathbf{r}, z) = b_g(z)\delta_m(\mathbf{r}, z), \quad (5)$$

where the bias b_g pertains to galaxies observed in the galaxy redshift survey. Generally, $b \neq b_g$ because intensity mapping and galaxy redshift surveys do not observe the same galaxy populations. This can be attributed to

different halo mass cutoffs for the two tracers (set by luminosity cutoffs in galaxy redshift surveys) and scatter in the probability a given halo will be populated by line-emitting gas or a directly-observable galaxy.

Figure 1 shows a comparison between the three realistic simulated fields δ_m , δ_I , and δ_g . Because δ_g traces δ_m , we can use it to measure the fluctuations in the density field, allowing us to remove the contributions from δ_m to cosmic variance in δ_I .

B. Cross-correlation statistics

The power spectrum of the intensity map is given by

$$P_I(\mathbf{k}, z) = T_I^2(\mathbf{k}, z) ([Ib]^2(z)P_m(k, z) + I_2(z)) + P_N(z), \quad (6)$$

where $P_m(z)$ is the matter power spectrum describing fluctuations in δ_m [32], \mathbf{k} the wavevector, and the wavenumber $k = |\mathbf{k}|$. The first (clustering) term is proportional to the square of the first moment of the luminosity function, along with a bias b . $I_2(z)$ is the shot power of the intensity map, and is proportional to the second moment of the galaxy luminosity function [33]:

$$I_2(z) = \alpha^2(z) \int_{M_{\min}}^{\infty} L^2(M, z) n(M, z) dM. \quad (7)$$

P_N represents the instrument noise, given by $P_N = \sigma_N^2 V_{\text{vox}}$ with $\sigma_N^2 = NEI^2/t_{\text{int}}$.

NEI is the noise-equivalent intensity given in units of $\text{Jy sr}^{-1} \text{s}^{1/2}$, V_{vox} is the voxel volume, and t_{int} is the integration time per pixel. The resolution transfer function, T_I , accounts for the loss of information on small scales due to finite spatial and frequency resolution in the intensity mapping instrument. We model T_I using a Gaussian profile, specified identically by e.g. Equation 13 in Bernal *et al.* [34].

For later convenience, we re-parameterize Equation 6 in terms of a dimensionless noise term W_I given by

$$W_I(\mathbf{k}, z) = \frac{I_2(z) + P_N(z)/T_I^2(\mathbf{k}, z)}{[Ib]^2(z)P_m(k, z)}, \quad (8)$$

with implied \mathbf{k}, z dependence, representing fractional noise in the intensity mapping measurement of the clustering power spectrum due to shot noise and instrument noise. W_I can be generalized to also include residual foregrounds and interloping lines. With this substitution, Equation 6 evaluates to

$$P_I(\mathbf{k}, z) = [Ib]^2(z)T_I^2(\mathbf{k}, z)P_m(k, z) [1 + W_I(\mathbf{k}, z)]. \quad (9)$$

We can analogously define the power spectra associated with the galaxy redshift survey, P_g , and the cross-correlation between the two surveys P_{\times} as

$$P_g(k, z) = b_g^2 P_m [1 + W_g(k, z)] \quad (10)$$

$$P_{\times}(\mathbf{k}, z) = T_I(\mathbf{k}, z)[Ib]b_g P_m [1 + W_{\times}(k, z)] \quad (11)$$

with associated dimensionless noise terms given by

$$W_g(k, z) = \frac{1}{\bar{n}(z)b_g^2(z)P_m(k, z)} \quad (12)$$

$$W_\times(k, z) = \frac{P_{\text{shot}}^\times(z)}{[Ib](z)b_g(z)P_m(k, z)}. \quad (13)$$

Here, \bar{n} represents the number density of galaxies observed in the galaxy redshift survey and P_{shot}^\times is the cross-shot power, representing correlated shot noise from the number of galaxies observed by both surveys. We estimate the cross-shot power as [33]

$$P_{\text{shot}}^\times(z) = \alpha(z) \int_{M_{\text{min}}^\times}^{\infty} L(M, z)n_g(M, z)n(M, z)dM, \quad (14)$$

where $n_g(M)$ is the halo occupation distribution of the galaxy redshift survey, which contributes to the number density of detected galaxies as $\bar{n} = \int_{M_{\text{min}}^g}^{\infty} n_g(M, z) n(M, z) dM$, with M_{min}^g the halo mass corresponding to the lower-luminosity threshold. M_{min}^\times is the minimum halo mass for galaxies observable in both surveys; we take $M_{\text{min}}^\times = M_{\text{min}}^g$ assuming the luminosity threshold in the galaxy redshift survey does not reach the smallest halos contributing to the [CII] intensity. Note that Equation 14 is approximate, as we have left out potentially important physics, such as scatter between the two galaxy populations, a soft cutoff for M_{min}^\times , and contributions from the 1-halo power spectrum. Later in the paper, we will explore marginalizing over P_{shot}^\times , leading to increased variance on small scales where the shot power is non-negligible compared to the clustering power spectrum.

We stress that the dimensionless noise parameters W_I , W_\times , and W_g are scale-dependent; on large scales where the clustering power spectra tend to dominate, the parameters tend to be much smaller than one. On small scales where instrument noise, shot power, and/or the 1-halo power spectrum dominate, the dimensionless noise parameters are larger than one, signifying increased variance in the maps.

C. Auto-correlation and cross-correlation sensitivities

We derive the sensitivity of the cross-correlation using the Fisher matrix formalism. We begin with the assumption that we can utilize information from all three maps: the intensity map, the galaxy map, and the cross-correlation map. In this case, the covariance matrix of the the intensity map and galaxy redshift survey is given by

$$\Sigma = \begin{pmatrix} P_I & P_\times \\ P_\times & P_g \end{pmatrix}. \quad (15)$$

and the Fisher matrix is given by Tegmark *et al.* [35]

$$F_{ij} = \frac{1}{2} \text{Tr} \left[\Sigma^{-1} \frac{\partial \Sigma}{\partial p_i} \Sigma^{-1} \frac{\partial \Sigma}{\partial p_j} \right], \quad (16)$$

where p_i corresponds to the varied parameters, e.g. $[Ib]$ and P_m .

As a first step, we calculate errors assuming information only in the line intensity map, i.e. the line intensity autocorrelation. Setting $\Sigma = P_I$ and inserting into Equation 16 with $p_i = [Ib]$, we arrive at the autopower errors,

$$\left. \frac{\sigma_{Ib}^2(\mathbf{k})}{(Ib)^2} \right|_{\text{auto}} = \frac{(1 + W_I(\mathbf{k}))^2}{2N_{\text{modes}}(\mathbf{k})}, \quad (17)$$

with N_{modes} the number of modes at a given wavenumber k . Note that z -dependence is implied. The first term in the parentheses describes the cosmic variance limit while the second describes variance in the map not originating from clustering of large-scale structure. Equation 17 is analogous to the Knox Formula describing errors in the cosmic microwave background [14], and the Feldman-Kaiser-Peacock Formula for errors in galaxy redshift surveys [36].

We can estimate the number of modes for a given wavenumber k and line of sight angle μ by using the isotropic mode-counting formula,

$$N_{\text{modes}}(\mathbf{k}) \approx \frac{k^2 V_{\text{surv}}}{8\pi^2} \delta k \delta \mu, \quad (18)$$

where μ is the angle of \mathbf{k} with respect to the line of sight, δk and $\delta \mu$ are the widths of the k and μ bins, and V_{surv} is the survey volume.

As a next step, we calculate errors in the inference of $[Ib]$ using information between both P_I and P_g , and the cross-correlation P_\times . Inserting the full covariance matrix (Equation 15) into the Fisher matrix, marginalizing over P_m , and varying over $[Ib]$, we arrive at the exact solution

$$\left. \frac{\sigma_{Ib}^2(\mathbf{k})}{[Ib]^2} \right|_\times = \frac{W_I - 2W_\times + W_g + W_I W_g - W_\times^2}{N_{\text{modes}}(\mathbf{k})}. \quad (19)$$

The cosmic variance term is no longer present, while there are additional contributions from W_\times and W_g . Note that W_\times contributes negatively to the fractional errors; this feature was pointed out by Liu and Breyse [7] studying constraints on f_{NL} using intensity mapping cross-power spectra. This effect can be contextualized through the map cross-correlation coefficient $\mathcal{R}_\times = (1 + W_\times) / \sqrt{(1 + W_I)(1 + W_g)}$. Cross-correlation errors are generally minimized when $\mathcal{R}_\times \rightarrow 1$, so increased correlated shot noise leads to decreased variance.

Finally, we stress that the variances listed in this section correspond to specific \mathbf{k} vectors, specified by a magnitude k and the cosine of the angle to the line-of-sight μ . Accurate variance per k must be performed by integrating Fisher matrices over μ , i.e. $F_{ij}(k) = \int d\mu F_{ij}(k, \mu)$. This is particularly important when factoring in RSD,

and in modes where the resolution transfer function approaches zero. μ -dependence enters the resolution transfer function because generally, the beam and frequency resolutions do not yield identical limits on perpendicular and parallel modes, respectively.

Note that while we focus on cross-correlation with galaxy redshift surveys, our formalism can be extended to other cross-correlations, including those between two intensity maps. However, this requires an understanding of correlated noise between the two maps and requires further study.

D. Robustness of the cross-correlation sensitivity

The qualitative features of the errors described by Equation 19 are robust to a variety of assumptions on the model and availability of data, namely, marginalizing over the cross-shot power, the non-inclusion of intensity mapping autocorrelation data, and additional sources of stochasticity in the cross-power spectrum.

1. Marginalizing over shot power and/or 1-halo terms in the cross-power spectrum

Our formalism for the cross-shot power given in Equation 14 is a rough estimate and leaves out many important details related to astrophysics and the 1-halo power spectrum. We therefore examine the conservative approach of marginalizing over P_{shot}^\times . Marginalizing over W_\times and P_m , Equation 19 instead evaluates exactly to

$$\left. \frac{\sigma_{Ib}^2(\mathbf{k})}{[Ib]^2} \right|_{P_{\text{shot}}^\times}^{\text{marg.}} = \frac{W_I - 2W_\times + W_g + \frac{1}{2}(W_I^2 + W_g^2) - W_\times^2}{N_{\text{modes}}(\mathbf{k})} \quad (20)$$

$$\left. \frac{\sigma_{P_{\text{shot}}^\times}^2(\mathbf{k})}{P_{\text{shot}}^2} \right|_{Ib}^{\text{marg.}} = \frac{2 - 2\tilde{W} + \tilde{W}^2/2}{N_{\text{modes}}(\mathbf{k})}, \quad (21)$$

where we have also solved for errors in the cross-shot power for completeness, and we have defined $\tilde{W} = (W_I + W_g)/W_\times$ for brevity. Note that here, cosmic variance contributes to the cross-power spectrum errors as a factor of $2/N_{\text{modes}}$.

Comparing Equation 20 to Equation 19, we find that terms linear in the W parameters are identical. We refer to these terms linear in W as the first-order errors. Higher-order terms, however, are different between the two surveys; terms quadratic in W_I and W_g appear. On small scales where the clustering power spectrum is subdominant in either the intensity or galaxy redshift survey maps (W_I or $W_g > 1$), marginalizing over P_{shot}^\times results in higher errors. On large scales where W_I and $W_g < 1$, marginalizing over P_{shot}^\times has little effect on the variance.

2. Exclusion of information from the auto-power of the intensity map

The covariance matrix in Equation 15 assumes that information is usable in both the intensity map and the galaxy redshift survey. In many cases, the intensity mapping autocorrelation signal can be contaminated by additive biases due to foregrounds, interloping lines, and other systematics. It is therefore useful to calculate errors assuming no information from the intensity map autocorrelation.

In this case, we define the data vector Θ by the two-point correlation functions defined by $\Theta = (P_\times, P_g)$. The covariance matrix is given by

$$\Sigma = \begin{pmatrix} C_{Ig}^{Ig} & C_{Ig}^{gg} \\ C_{Ig}^{gg} & C_{gg}^{gg} \end{pmatrix} \quad (22)$$

where $C_{Ig}^{Ig} = P_\times^2 + P_I P_g$, $C_{Ig}^{gg} = 2P_\times P_g$, and $C_{gg}^{gg} = 2P_g^2$ are the covariances per mode, assuming Gaussian fields in δ_I and δ_g .

Using the Fisher matrix for information in the mean (rather than the covariance),

$$F_{ij} = \frac{1}{2} \text{Tr} \left[\Sigma^{-1} \left(\frac{\partial \Theta^T}{\partial p_i} \frac{\partial \Theta}{\partial p_j} + \frac{\partial \Theta^T}{\partial p_j} \frac{\partial \Theta}{\partial p_i} \right) \right], \quad (23)$$

and plugging Equation 21 and Θ into Equation 23, we again find that the first-order sensitivity in $[Ib]$ is identical to that shown in Equation 19, with differences appearing at second-order:

$$\left. \frac{\sigma_{Ib}^2(\mathbf{k})}{[Ib]^2} \right|_\times = \frac{W_I - 2W_\times + W_g}{N_{\text{modes}}} + \frac{W_I W_g - 4W_\times W_g + W_\times^2 + 2W_g^2}{N_{\text{modes}}}. \quad (24)$$

Cosmic variance is still suppressed because P_m can be marginalized over through P_\times and P_g .

For a final case, we calculate errors including only information from the cross-correlation P_\times . Using a covariance $\Sigma = C_{Ig}^{Ig}$ and data $\Theta = P_\times$ and plugging into Equation 23, we arrive at

$$\left. \frac{\sigma_{Ib}^2(\mathbf{k})}{[Ib]^2} \right|_{\times \text{ only}} = \frac{1}{N_{\text{modes}}} + \frac{(1 + W_I)(1 + W_g)}{N_{\text{modes}}(1 + W_\times)^2}. \quad (25)$$

Here, cosmic variance variance has re-appeared because it is not possible to marginalize over P_m .

3. Additional sources of stochasticity

The galaxy redshift survey and intensity mapping survey may not identically trace the underlying matter field. We benchmark this effect through a cross-correlation (stochasticity) coefficient r_\times , contributing to the cross-power spectrum as

$$P_\times^r = [Ib] b_g P_m [r_\times + W_\times]. \quad (26)$$

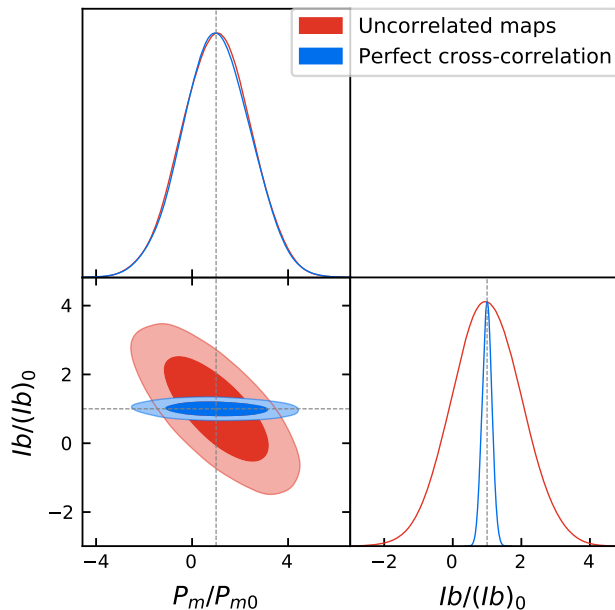


FIG. 2. Illustration of cosmic variance evasion technique for a single mode in the cross-power spectra given by Equation 27 with noise parameters arbitrarily chosen as $(W_I, W_\times, W_g) = (0.01, 0, 0.01)$. The red ellipse shows the case where $r_\times = 0$, i.e. the maps are uncorrelated, resulting in a variance-limited measurement in $[Ib]$. Here, measurements of $Ib/(Ib)_0$ and P_m/P_{m0} are degenerate in P_I , resulting in coupling between errors in the P_m and $[Ib]$. The blue ellipse shows the $r_\times = 1$ case, where we are able to flatten the covariance ellipse in the $Ib/(Ib)_0 - P_m/P_{m0}$ plane, allowing us to marginalize the P_m errors with minimal residual errors.

This is purely a choice of convention, as all sources of decorrelation can also be absorbed into W_\times and marginalized or measured. Marginalizing over W_\times and P_m , residual stochasticity contributes to the fractional variance in the cross-power (analogous to Equation 20) as

$$\frac{\sigma_{Ib}^2(\mathbf{k})}{[Ib]^2} \Big|_{r_\times} = \frac{1 - r_\times^2 - 2r_\times W_\times + W_I + W_g}{N_{\text{modes}}(\mathbf{k})} + \frac{-W_\times^2 + (W_I^2 + W_g^2)/2}{N_{\text{modes}}(\mathbf{k})}. \quad (27)$$

Note that cosmic variance appears when the cross-correlation coefficient $r_\times \neq 1$, and Equation 20 is recovered in the limit that $r_\times \rightarrow 1$. In the limit that $r_\times \rightarrow 0$, we recover a cosmic variance term as in Equation 17. Note that nonlinear processes that cause $r_\times < 1$ tend to appear on small scales, similar to those where the shot power becomes dominant; effects include scale-dependent biases and contributions to the 1-halo power spectrum that may be incorrectly modeled.

Equation 27 is useful to illustrate the importance of highly-correlated maps in canceling cosmic variance. Figure 2 shows error contours for a single mode in the $[Ib]$ -

P_m plane for two cases: perfectly uncorrelated maps ($r_\times = 0$), and perfectly correlated maps ($r_\times = 1$). In the uncorrelated case, the degeneracy between P_m and $[Ib]$ is shown clearly in the error ellipse; cosmic variance errors in P_m are coupled to errors in $[Ib]$. Note, however, that the degeneracy is mildly broken by the appearance of P_m in the clustering power of the galaxy redshift survey. In the perfectly correlated case, the degeneracy is broken and errors in $[Ib]$ are no longer coupled to those in P_m , so errors in the former are limited by noise in the maps, rather than cosmic variance.

III. DESIGNING AN INTENSITY MAPPING SURVEY WITHOUT COSMIC VARIANCE

A. Survey optimization

Given a fixed total time for a survey, Equations 17 and 19 can be used to optimize the total survey area A_{surv} , in order to reduce errors in a given k . Throughout this section we assume W_I is dominated by instrument noise, rather than shot noise or residual foregrounds. Increased integration time per pixel linearly decreases instrument noise and therefore W_I . However, the increased integration time per pixel results in a smaller number of observed pixels, linearly decreasing the scan area A_{surv} and therefore N_{modes} . Different terms present in Equations 17 and 19 scale with survey area (with fixed total survey time) as

$$\begin{aligned} \frac{1}{N_{\text{modes}}} &\propto A_{\text{surv}}^{-1} \\ \frac{W_I}{N_{\text{modes}}} &\propto A_{\text{surv}}^0 \\ \frac{W_I^2}{N_{\text{modes}}} &\propto A_{\text{surv}}^1. \end{aligned} \quad (28)$$

Errors in the autocorrelation scale analogously to conclusions made in Knox [14]. When instrument noise dominates, there is a clear preference for small survey coverage with increased integration time per pixel. This is because, for an instrument noise-dominated survey, autocorrelation errors are proportional to W_I^2/N_{modes} , which increase linearly with A_{surv} . When $W_I < 1$, i.e. when cosmic variance dominates the errors, it is best to widen the survey area. We therefore suggest optimizing the integration time per pixel for autocorrelation so that W_I is just below 1, over the widest area possible.

Cross-correlation errors scale slightly differently from autocorrelation errors. When we do not marginalize over W_\times , Equation 19 shows that W_I does not contribute beyond linear order. Based on the scaling of W_I with N_{modes} , this would suggest no preference for wide or deep surveys when instrument noise dominates, but again, a clear preference for wide surveys when $W_I < 1$. On the other hand, if we marginalize over the cross-shot power,

Equation 20 shows that the variance is quadratic in W_I , increasing proportionally to A_{surv} ; thus, a deep survey is preferred. Generally, however, deep surveys emphasize high- k modes, putting more weight on the modes where correlated shot modes is marginalized.

In the case where instrument noise is low, errors in the cross-power are not cosmic variance-limited. Instead, errors are limited by W_g , as described in Equations 19 and 20. Therefore, it is ideal to set the integration time such that the depths of the two surveys match, i.e. $W_I \approx W_g$. Increasing the integration time beyond this limit would only decrease W_I while W_g remains constant; increasing A_{surv} , on the other hand, would increase N_{modes} , thereby decreasing errors attributed to both W_I and W_g . This survey strategy extends the arguments of Knox [14] to the cross-power; errors in the cross-correlation are limited by noise in the galaxy redshift survey, rather than cosmic variance.

B. Realistic survey model

We benchmark our model by producing a realistic intensity mapping cross-correlation strategy for a realistic cross-correlation between a space-based [CII] line-intensity mapping survey and the nominal 2000 deg² High-Latitude Survey for the Nancy Grace Roman Space Telescope [37] at $z = 1.5$.

The rest frequency of [CII] is $\nu_{\text{CII}}^{\text{rest}} = 1900$ GHz. We calculate the [CII] intensity by inserting the mass-luminosity function of Padmanabhan [38] into Equations 2 and 4, resulting in a biased intensity of $[Ib](z = 1.5) = 144 \text{ Jy sr}^{-1}$. We model the Roman HOD through HOD0 in [39], with a multiplicative constant scaled to obtain an average galaxy number density of $\bar{n}(z = 1.5) = 0.0016 \text{ h}^3 \text{ Mpc}^{-3}$, and we calculate a bias $b_g(z = 1.5) = 2.3$.

We assume a $1/e$ beamwidth of 1 arcmin corresponding to a 70 cm primary mirror, and a spectral resolving power $R = 500$, resulting in a frequency resolution $\delta\nu = 1.27$ GHz, which we take to be equal to the single-channel bandwidth.

We assume the noise in the intensity map is background-limited with a background intensity of $I_{\text{bknd}} = 9 \times 10^3 \text{ kJy sr}^{-1}$, an accurate figure for the combined CMB, galactic Cirrus in typical clean regions out of the galactic plane, and CIB radiation [40–42]. Our strategy to calculate the NEI is to first relate I_{bknd} to the power absorbed by the detectors P_{det} , through the relation $P_{\text{det}} = \eta_{\text{det}} I_{\text{bknd}} \partial P / \partial I$, with η_{det} the detector efficiency and $\partial P / \partial I = A_d \Omega_{\text{inst}} \delta\nu$, assuming an unpolarized source.

Here, the detector area A_d and the beam area Ω_{inst} are related to the frequency $\nu = 760$ GHz and number of optical modes N_{opt} as $A_d \Omega_{\text{inst}} = N_{\text{opt}} \eta_{\text{opt}} (c/\nu)^2$, with η_{opt} the optical efficiency. We assume $N_{\text{opt}} = 1$ and $\eta_{\text{opt}} \eta_{\text{det}} = 0.20$. The resulting detector power is translated into a photon background-limited noise-equivalent

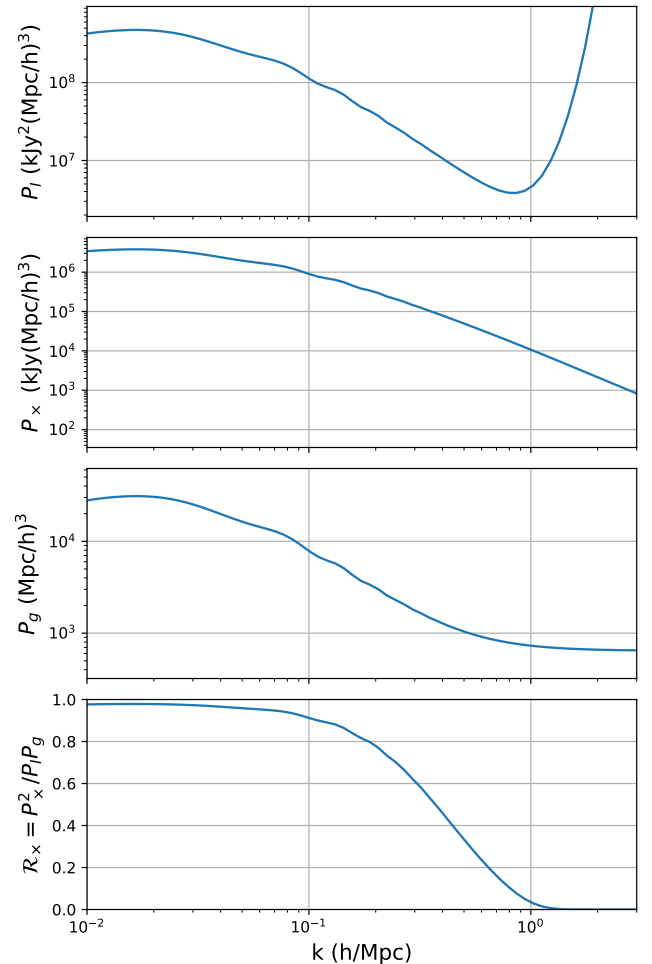


FIG. 3. Power spectra corresponding to the wide survey model in III B: intensity mapping auto-power spectrum (top), cross-power spectrum (upper middle), galaxy auto-power spectrum (lower middle), and map-space cross-correlation coefficient (bottom).

power $NEP = [h\nu P_{\text{det}} + P_{\text{det}}^2 / \delta\nu]^{1/2}$ (e.g. [43]), where h is Planck's constant. This results in $NEP = 4.6 \times 10^{-20} \text{ W Hz}^{-1/2}$, a realistic goal for, e.g. far-infrared kinetic inductance detectors [44, 45]. Finally, we calculate $NEI = NEP / \eta_{\text{det}} / (\sqrt{2} \partial P / \partial I) = 69.2 \text{ kJy sr}^{-1}$. The factor of $\sqrt{2}$ comes from the conversion from power spectral conventions of $\text{Hz}^{1/2}$ to $\text{s}^{-1/2}$. The model survey occupies 2000 deg² over a range of redshift $\Delta z = 0.2$ over 417 days, (5 s per $1/e$ beamwidth) resulting in $V_{\text{surv}} = 1.4 \text{ h}^{-3} \text{ Gpc}^3$.

The resulting power spectra are shown in Figure 3, and sensitivities are shown in Figure 4. The latter shows the fractional variance per k given three cases: autopower, cross-power errors using information from the cross-power only (labeled CV), and cross-power errors using information from all available maps, marginalized over P_m and P_x^{shot} ; these errors are calculated by Equations 17, 25, and 20, respectively. We marginalize over

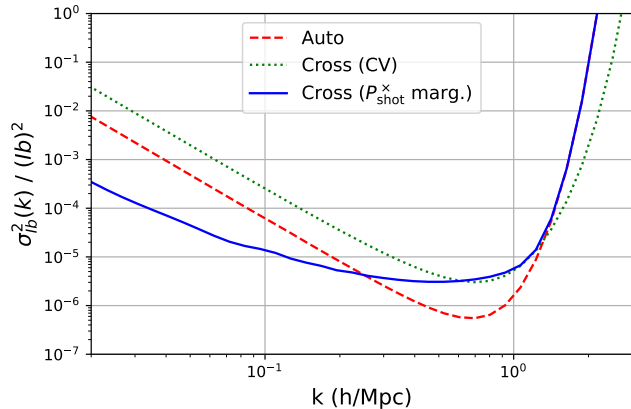


FIG. 4. Fractional variance per mode in $[Ib]$. We model errors in the intensity map autocorrelation, and cross-correlation marginalized over P_{shot}^{\times} , specified by Equations 17 and 20, respectively. The instrument design is specified in Section III B.

P_{\times}^{shot} in the latter case to remain conservative about our simplified model describing Equation 14. We assume 32 bandpowers in k spanning $0.01 < k < 2.7 \text{ hMpc}^{-1}$ equally spaced logarithmically, with Fisher matrices integrated over μ . We note that instrument noise dominates shot power, and we assume sufficient bandpass stability that noise due to residual foregrounds is also subdominant.

The cosmic variance-evading cross-power significantly outperforms the autopower and cross (CV) errors on large scales where the intensity and galaxy redshift survey maps are highly-correlated, i.e. $\mathcal{R}_{\times} \approx 1$. On smaller scales ($k \gtrsim 0.3 \text{ hMpc}^{-1}$), autopower errors outperform crosspower errors because dimensionless noise in the galaxy redshift survey exceeds cosmic variance, i.e. $W_g > 1$. The cross (CV) case also outperforms the marginalized cross-power on smaller scales ($k \gtrsim 1.1 \text{ hMpc}^{-1}$) because the latter is marginalized over the P_{shot}^{\times} , thereby increasing errors.

Figure 5 shows variance per k as a function of survey area, assuming the same total survey time. We calculate the variance for two modes: $k = 0.02$ and 0.80 hMpc^{-1} . Variance in the 0.02 hMpc^{-1} mode is minimized by increasing A_{surv} as much as possible. This is because $W_I < W_g$ even for the largest survey area, so increased survey depth does little to decrease variance in $[Ib]$. Furthermore, on these large scales the cross-power provides a drastic increase in sensitivity compared to the cosmic variance-limited autopower.

For $k = 0.80 \text{ hMpc}^{-1}$ modes, the autopower produces smaller errors than the cross-power for almost all survey depths. Here, noise in the galaxy redshift survey exceeds cosmic variance, i.e. $W_g > 1$. For the largest survey areas, however, the crosspower performs similarly to the autopower. Though we marginalize over the cross-shot power, care must be taken to understand nonlinear

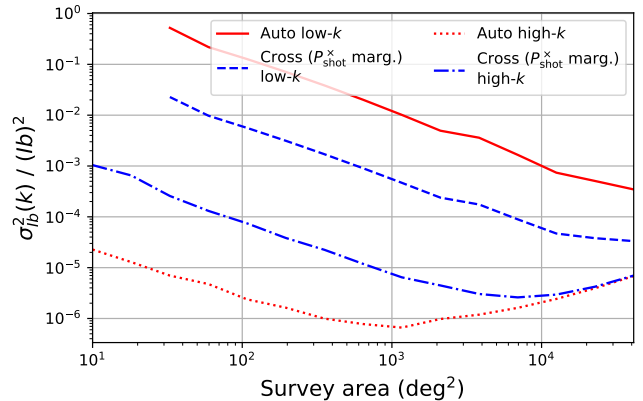


FIG. 5. Fractional variance per mode in $[Ib]$ varying the survey area from 10 to 40000 deg^2 (full-sky) at fixed survey time.

physics on these scales to validate this conclusion. The autocorrelation variance for $k = 0.80 \text{ hMpc}^{-1}$ is minimized for $A_{\text{surv}} \approx 1100 \text{ deg}^2$. This corresponds to the survey depth that matches cosmic variance, i.e. $W_I \approx 1$, matching conclusions described in Knox [14]. The cross-correlation variance features a similar minimum instead at $A_{\text{surv}} \approx 10,000 \text{ deg}^2$. On this scale, the depth of the intensity map matches that of the galaxy redshift survey, i.e. $W_I \approx W_g$. Finally, we note that in the case of increased noise in the intensity map, these minima would be pushed to proportionally smaller survey areas.

IV. CONCLUSION

Intensity mapping cross-correlations provide a powerful means to measuring the biased intensity of a given tracer. Cross-correlation has well-established utility to reject sources of contamination in the intensity map that are not correlated with the target galaxy population, such as interlopers and foregrounds [8–10]. Furthermore, cross-correlation measurements of the biased intensity can evade cosmic variance.

For a given k mode, cosmic variance can be mitigated if the fractional noise in the clustering power spectrum in both surveys (i.e. W_I and W_g) is less than 1, and if the stochasticity between the surveys is small. These requirements are straightforwardly achieved on large, linear scales. Smaller scales tend to feature higher fractional noise and higher stochasticity due to the dominance of nonlinear physics. On smaller scales, an intensity mapping autocorrelation may be preferable to a cross-correlation, because the latter introduces an additional source of noise from the cross-correlating survey, which may exceed cosmic variance. Note, however, that the use of the autocorrelation requires stronger control of contamination from foregrounds and interlopers. In either case, the depth of the intensity map is optimized when fractional noise in the intensity map matches that

of the cross-correlating survey. We stress that this optimal depth depends on the scales of interest and the level of noise in the two surveys. There is therefore no one-size-fits-all optimum survey depth, but careful analyses using the techniques and equations described in this paper provide a useful framework for designing a survey to achieve specific science goals.

V. ACKNOWLEDGEMENTS

We thank Patrick Breyse and Anthony Pullen for useful discussion about LIM cross-correlations and careful review of the draft, and David Leisawitz for discussion on the mid- to far-IR photon background. TMO especially thanks Peter Timbie for invaluable guidance and advising. We also thank our reviewer for useful comments. TMO thanks the Wisconsin Space Grant for fellowship support, the National Space Grant and Universities Space Research Association for internship support, and the UW-Madison graduate school for training and support. We acknowledge the use of the `astropy`, `colossus` [32], `matplotlib`, and `numpy` Python modules.

-
- [1] E. R. Switzer, *The Astrophysical Journal* **838**, 82 (2017).
- [2] A. Slosar, Z. Ahmed, D. Alonso, M. A. Amin, E. J. Arena, K. Bandura, N. Battaglia, J. Blazek, P. Bull, E. Castorina, *et al.*, *Bulletin of the American Astronomical Society* **51**, 53 (2019).
- [3] E. Schaan and M. White, *Journal of Cosmology and Astroparticle Physics* **2021** (05), 067.
- [4] J.-M. Alimi, D. Valls-Gabaud, and A. Blanchard, *Astronomy and Astrophysics* **206**, L11 (1988).
- [5] E. D. Kovetz, M. P. Viero, A. Lidz, L. Newburgh, M. Rahman, E. Switzer, M. Kamionkowski, J. Aguirre, M. Alvarez, J. Bock, *et al.*, arXiv preprint arXiv:1709.09066 (2017).
- [6] E. Switzer, C. Anderson, A. Pullen, and S. Yang, *The Astrophysical Journal* **872**, 82 (2019).
- [7] R. H. Liu and P. C. Breyse, *Physical Review D* **103**, 063520 (2021).
- [8] E. Switzer, K. Masui, K. Bandura, L.-M. Calin, T.-C. Chang, X.-L. Chen, Y.-C. Li, Y.-W. Liao, A. Natarajan, U.-L. Pen, *et al.*, *Monthly Notices of the Royal Astronomical Society: Letters* **434**, L46 (2013).
- [9] R. A. Croft, J. Miralda-Escudé, Z. Zheng, M. Blomqvist, and M. Pieri, *Monthly Notices of the Royal Astronomical Society* **481**, 1320 (2018).
- [10] S. Yang, A. R. Pullen, and E. R. Switzer, *Monthly Notices of the Royal Astronomical Society: Letters* **489**, L53 (2019).
- [11] L. R. Abramo and K. E. Leonard, *Monthly Notices of the Royal Astronomical Society* **432**, 318 (2013).
- [12] G. M. Bernstein and Y.-C. Cai, *Monthly Notices of the Royal Astronomical Society* **416**, 3009 (2011).
- [13] U. Seljak, *Physical Review Letters* **102**, 021302 (2009).
- [14] L. Knox, *Physical Review D* **52**, 4307 (1995).
- [15] C. Carilli and F. Walter, *Annual Review of Astronomy and Astrophysics* **51**, 105 (2013).
- [16] A. M. Dizgah and G. K. Keating, *The Astrophysical Journal* **872**, 126 (2019).
- [17] A. R. Pullen, P. Serra, T.-C. Chang, O. Doré, and S. Ho, *Monthly Notices of the Royal Astronomical Society* **478**, 1911 (2018).
- [18] G. Stacey, M. Aravena, K. Basu, N. Battaglia, B. Beringue, F. Bertoldi, J. Bond, P. Breyse, R. Bustos, S. Chapman, *et al.*, in *Ground-based and Airborne Telescopes VII*, Vol. 10700 (International Society for Optics and Photonics, 2018) p. 107001M.
- [19] P. Ade, M. Aravena, E. Barria, A. Beelen, A. Benoit, M. Béthermin, J. Bounmy, O. Bourrion, G. Bres, C. De Breuck, *et al.*, *Astronomy & Astrophysics* **642**, A60 (2020).
- [20] G. Cataldo, P. A. Ade, C. J. Anderson, A. Barlis, E. M. Barrentine, N. G. Bellis, A. D. Bolatto, P. C. Breyse, B. T. Bulcha, J. A. Connors, *et al.*, in *Ground-based and Airborne Telescopes VIII*, Vol. 11445 (International Society for Optics and Photonics, 2020) p. 1144524.
- [21] J. Vieira, J. Aguirre, C. M. Bradford, J. Filippini, C. Groppi, D. Marrone, M. Bethermin, T. C. Chang, M. Devlin, O. Dore, *et al.*, in *2019 30th International Symposium on Space Terahertz Technology, ISSTT 2019* (2019).
- [22] G. Sun, T.-C. Chang, B. D. Uzgil, J. Bock, C. M. Bradford, V. Butler, T. Caze-Cortes, Y.-T. Cheng, A. Cooray, A. T. Crites, *et al.*, *The Astrophysical Journal* **915**, 33 (2021).
- [23] A. Kogut, D. T. Chuss, J. Dotson, E. Dwek, D. J. Fixsen, M. Halpern, G. F. Hinshaw, S. Meyer, S. H. Moseley, M. D. Seiffert, *et al.*, in *Space Telescopes and Instrumentation 2014: Optical, Infrared, and Millimeter Wave*, Vol. 9143 (International Society for Optics and Photonics, 2014) p. 91431E.
- [24] J. Glenn, C. M. Bradford, R. Amini, B. Moore, A. Benson, L. Armus, K. Alatalo, J. Darling, P. Day, J. Domber, *et al.*, in *Space Telescopes and Instrumentation 2018: Optical, Infrared, and Millimeter Wave*, Vol. 10698 (International Society for Optics and Photonics, 2018) p. 106980L.
- [25] D. Leisawitz, E. G. Amatuucci, L. N. Allen, J. W. Arenberg, L. Armus, C. Battersby, J. M. Bauer, P. Beltran, D. J. Benford, D. Burgarella, *et al.*, *Journal of Astronomical Telescopes, Instruments, and Systems* **7**, Art (2021).
- [26] A. Cooray and R. Sheth, *Physics reports* **372**, 1 (2002).
- [27] P. Serra, G. Lagache, O. Doré, A. Pullen, and M. White, *Astronomy & Astrophysics* **570**, A98 (2014).
- [28] M. Viero, L. Wang, M. Zemcov, G. Addison, A. Amblard, V. Arumugam, H. Aussel, M. Béthermin, J. Bock, A. Boselli, *et al.*, *The Astrophysical Journal* **772**, 77 (2013).
- [29] C. Shang, Z. Haiman, L. Knox, and S. P. Oh, *Monthly Notices of the Royal Astronomical Society* **421**, 2832

- (2012).
- [30] R. K. Sheth and G. Tormen, Monthly Notices of the Royal Astronomical Society **329**, 61 (2002).
- [31] J. L. Tinker, B. E. Robertson, A. V. Kravtsov, A. Klypin, M. S. Warren, G. Yepes, and S. Gottlöber, The Astrophysical Journal **724**, 878 (2010).
- [32] B. Diemer, The Astrophysical Journal Supplement Series **239**, 35 (2018).
- [33] P. C. Breysse and R. M. Alexandroff, Monthly Notices of the Royal Astronomical Society **490**, 260 (2019).
- [34] J. L. Bernal, P. C. Breysse, H. Gil-Marín, and E. D. Kovetz, Physical Review D **100**, 123522 (2019).
- [35] M. Tegmark, A. N. Taylor, and A. F. Heavens, The Astrophysical Journal **480**, 22 (1997).
- [36] H. A. Feldman, N. Kaiser, and J. A. Peacock, The Astrophysical Journal **426**, 23 (1994).
- [37] O. Doré, C. Hirata, Y. Wang, D. Weinberg, I. Baronchelli, A. Benson, P. Capak, A. Choi, T. Eifler, S. Hemmati, *et al.*, arXiv e-prints , arXiv (2018).
- [38] H. Padmanabhan, Monthly Notices of the Royal Astronomical Society **488**, 3014 (2019).
- [39] A. Smith, E. Burtin, J. Hou, R. Neveux, A. J. Ross, S. Alam, J. Brinkmann, K. S. Dawson, S. Habib, K. Heitmann, *et al.*, Monthly Notices of the Royal Astronomical Society **499**, 269 (2020).
- [40] D. Fixsen, E. Cheng, J. Gales, J. C. Mather, R. Shafer, and E. Wright, The Astrophysical Journal **473**, 576 (1996).
- [41] D. Fixsen, E. Dwek, J. C. Mather, C. Bennett, and R. Shafer, The Astrophysical Journal **508**, 123 (1998).
- [42] A. Bracco, A. Cooray, M. Veneziani, A. Amblard, P. Serra, J. Wardlow, M. Thompson, G. White, R. Auld, M. Baes, *et al.*, Monthly Notices of the Royal Astronomical Society **412**, 1151 (2011).
- [43] J. Zmuidzinas, Applied optics **42**, 4989 (2003).
- [44] J. Baselmans, J. Bueno, S. J. Yates, O. Yurduseven, N. Llombart, K. Karatsu, A. Baryshev, L. Ferrari, A. Endo, D. Thoen, *et al.*, Astronomy & Astrophysics **601**, A89 (2017).
- [45] C. M. Bradford, B. A. Cameron, B. D. Moore, S. Hailey-Dunsheath, E. G. Amatucci, D. C. Bradley, J. A. Corsetti, D. T. Leisawitz, M. J. DiPirro, J. G. Tuttle, *et al.*, Journal of Astronomical Telescopes, Instruments, and Systems **7**, 011017 (2021).